bioRxiv preprint doi: https://doi.org/10.1101/2024.04.02.587715; this version posted April 2, 2024. The copyright holder for this preprint (which was not certified by peer review) is the author/funder. All rights reserved. No reuse allowed without permission.

# Mid-infrared photoacoustic brain imaging enabled by cascaded gas-filled hollow-core fiber lasers

**Cuiling Zhang,[a] Kunyang Sui,[a,b] Marcello Meneghetti,[a,b] Jose Enrique Antonio-Lopez,[c] Manoj K. Dasa,[d] Rune W. Berg,[b] Rodrigo Amezcua-Correa,[c] Yazhou Wang,[a] and Christos Markos,[a,e,*]**

[a]DTU Electro, Technical University of Denmark, 2800 Kgs. Lyngby, Denmark
[b]Department of Neuroscience, University of Copenhagen, 2200 Copenhagen, Denmark
[c]CREOL, The College of Optics and Photonics, University of Central Florida, 32816 Orlando, Florida, USA
[d]NKT Photonics A/S, Blokken 84, 3460 Birkerød, Denmark
[e]NORBLIS ApS, Virumgade 35D, 2830 Virum, Denmark

**Abstract**

**Significance:** Extending the photoacoustic microscopy (PAM) into the mid-infrared (MIR) molecular fingerprint region constitutes a promising route towards label-free imaging of biological molecular structures. Realizing this objective requires a high-energy nano-second MIR laser source. However, existing MIR laser technologies are limited to either low pulse energy or free-space structure which is sensitive to environmental conditions. Fiber lasers are promising technologies for PAM for their potential of offering both high pulse energy and robust performance against environmental conditions. However, MIR high energy fiber laser has not yet been used for PAM because it is still at the infant research stage.

**Aim:** We aim to employ the emerging gas-filled anti-resonant hollow-core fiber (ARHCF) laser technology for MIR-PAM for the purpose of imaging myelin-rich regions in a mouse brain.

**Approach:** This laser source is developed with a ~2.75 μJ high-pulse-energy nano-second laser at 3.4 μm, targeting the main absorption band of myelin sheaths, the primary chemical component of axons in the central nervous system. The laser mechanism relies on two-orders gas-induced vibrational stimulated Raman scattering (SRS) for nonlinear wavelength conversion, starting from a 1060 nm pump laser to 1409 nm through the 1$^{st}$ order Stokes generation in the nitrogen-filled 1$^{st}$ stage ARHCF, then, from 1409 nm to 3.4 μm through the 2$^{nd}$ stage hydrogen-filled ARHCF.

**Results:** The developed Raman laser was used for the first time for transmission-mode MIR-PAM of mouse brain regions containing rich myelin structures.

**Conclusions:** This work pioneers the potential use of high-energy and nano-second gas-filled ARHCF laser source to MIR-PAM, with a first attempt to report this kind of fiber laser source for PAM of lipid-rich myelin regions in a mouse brain. The proposed ARHCF laser technology is also expected to generate high-energy pulses at the ultraviolet (UV) region, which can significantly improve the lateral resolution of the PAM.

**Keywords**: photoacoustic microscopy, lipids, myelin, mid-infrared, gas-filled hollow core fiber laser

***** E-mail: chmar@dtu.dk

## 1 Introduction

Photoacoustic microscopy (PAM) is a prominent non-invasive imaging modality that uses optical excitation to generate ultrasound signals, allowing the visualization of biomedical tissues,

bioRxiv preprint doi: https://doi.org/10.1101/2024.04.02.587715; this version posted April 2, 2024. The copyright holder for this preprint (which was not certified by peer review) is the author/funder. All rights reserved. No reuse allowed without permission.

inorganic materials, or complex samples with larger penetration depths when compared to other optical imaging techniques [1–4]. In recent years, PAM within the visible and near-infrared (NIR) wavelength regions have unveiled a wealth of functional information, contributing to advancements in various research fields [5–9]. Currently, the scientific community focuses on moving PAM technology to the mid-infrared (MIR) wavelength domain, opening the door to new opportunities in microscopy with emphasis on probing specific molecular vibrational bands, such as those associated with $CH_2$ groups [10–15]. For instance, He *et.al.* reported the use of mid-infrared photoacoustic microscopy (MIR-PAM) for mapping the lipid compositions ($CH_2$ stretching transition) in mouse brain and kidney tissue at ~3.4 μm [10]. Furthermore, MIR-PAM enabled the imaging of carbohydrates (at ~9.2 μm), lipids (at ~3.5 μm), and proteins (at ~6.4 μm) in living cells and tissues [11,12]. Compared with the NIR-PAM, the lateral resolution of the MIR-PAM is diffraction-limited to the long wavelength of the MIR laser. This challenge was recently addressed by adding an ultraviolet (UV) pulsed laser as a probe, to enhance the PAM resolution down to the nanometer scale to image lipids, proteins, and nucleic acids [13].

Quantum-cascaded lasers (QCLs) and optical parametric oscillators (OPOs) are the main light sources that have been used for MIR-PAM because mainly of their broad wavelength selectivity [10–15]. However, QCL technology is limited by low peak power of only few watts, leading to a low pulse energy of only few nanojoule at even tens of nanosecond pulse duration [11,14-15]. Some efforts have been made to circumvent this issue, including mitigating the laser energy attenuation caused by the ambient gas absorption such as creating a nitrogen ($N_2$)-filled atmosphere, and prolonging the pulse duration to tens of nanosecond. Based on these methods, QCL has been used for scanning-mode-based PAM, however, the pulse energy is too low to be used for real-time PA modalities [14-16]. OPO technology, on the other hand, can deliver high

bioRxiv preprint doi: https://doi.org/10.1101/2024.04.02.587715; this version posted April 2, 2024. The copyright holder for this preprint (which was not certified by peer review) is the author/funder. All rights reserved. No reuse allowed without permission.

pulse energy of tens microjoule. However, its free-space structure [10] introduces practical limitations due to its sensitivity on environmental conditions such as vibrations, humidity, and temperature.

Fiber lasers are promising alternatives for PA technology because they have the potential to deliver both high pulse energy and robust performance against environmental conditions. Driven by these advantages, mature visible and NIR fiber laser technologies have been recently proposed for PA technology [17-20]. However, MIR high-energy fiber lasers have not yet been used for PAM. In this work, we developed a novel MIR fiber laser technology for PA imaging for the first time. Specifically, the fiber laser emits high energy nanosecond pulses at the absorption peak of myelin at 3.4 μm wavelength to image the neurons in the brain slice [10,12]. The mechanism of the proposed laser is based on the stimulated Raman scattering (SRS) in gas-filled anti-resonant hollow-core fiber (ARHCF), which is an emerging fiber technology, that allows confinement of the laser beam within its hollow region resulting in very strong light-gas (atomic or molecular) interactions (thus efficient SRS frequency) [21,22]. This property not only enables the generation of strong pulses over a broad wavelength range from ultraviolet (UV) to MIR (as summarized in Table S1) [23–28], but also is not limited from the damage threshold of the glass. Therefore, compared to other nonlinear media, gases are considered, in a sense, self-healing, unlike solids which can become permanently damaged [22] and thus allowing energy and intensity scaling of nonlinear devices to their most extreme limit [29]. This highlights its potential to broaden the spectral range beyond the existing fiber lasers utilized in PAM, such as standard doped silica fibers [17-19].

bioRxiv preprint doi: https://doi.org/10.1101/2024.04.02.587715; this version posted April 2, 2024. The copyright holder for this preprint (which was not certified by peer review) is the author/funder. All rights reserved. No reuse allowed without permission.

## 2 Material and methods

Figure 1 shows the configuration of the entire system combining the proposed MIR gas-filled fiber laser source and the PAM.

### *2.1 Cascaded gas-filled ARHCF laser*

The MIR gas-filled fiber Raman laser source at 3.4 μm is based on a configuration of cascading two gas-filled ARHCFs. To efficiently convert the conventional NIR to the MIR at the selected 3.4 μm wavelength, here the 2$^{nd}$ stage ARHCF is filled with pure $H_2$, offering a long vibrational Raman Stokes (VRS) coefficient of 4155 cm$^{-1}$, and also a relatively high gain coefficient compared with other Raman active gases [34]. This requires a pump wavelength at ~1.4 μm, which is outside the gain range of the known rare-earth ion-based fibers. Therefore, we first generated the required ~1.4 μm laser by using the 1$^{st}$ order VRS (2331 cm$^{-1}$) of $N_2$ in the 1$^{st}$ ARHCF stage [35], pumped by a Yb-doped fiber laser at 1 μm region. The pump laser has an all-fiber structure consisting of a modulated diode laser seed followed by an Yb-doped fiber amplification module, emitting a pulse train with a repetition rate of 1.2 kHz, ~3.7 ns pulse duration, energy of ~98 μJ (measured by an energy meter, PE9-ES-C, Ophir Optronics), and 0.128 nm linewidth at 1060 nm wavelength [36]. A λ/2 waveplate is placed at the output of the amplifier for adjusting the polarization orientation to acquire the highest Raman conversion efficiency in the subsequent gas-filled ARHCF system. Then the beam is coupled into the $N_2$-filled ARHCF to generate the 1$^{st}$ order VRS line at 1409 nm [35], which is then used as a pump for the 2$^{nd}$ stage ARHCF, to generate the Raman laser at MIR 3.4 μm wavelength.

The scanning electron microscopy (SEM) images of the two ARHCFs used in our experiments are shown in Fig. 1. The first stage ARHCF (Fiber 1 in Fig. 1) is a 16-meters-long single-ring nodeless ARHCF, consisting of 7 rings with a diameter of 16.1 μm and wall thickness of ~323 nm,

bioRxiv preprint doi: https://doi.org/10.1101/2024.04.02.587715; this version posted April 2, 2024. The copyright holder for this preprint (which was not certified by peer review) is the author/funder. All rights reserved. No reuse allowed without permission.

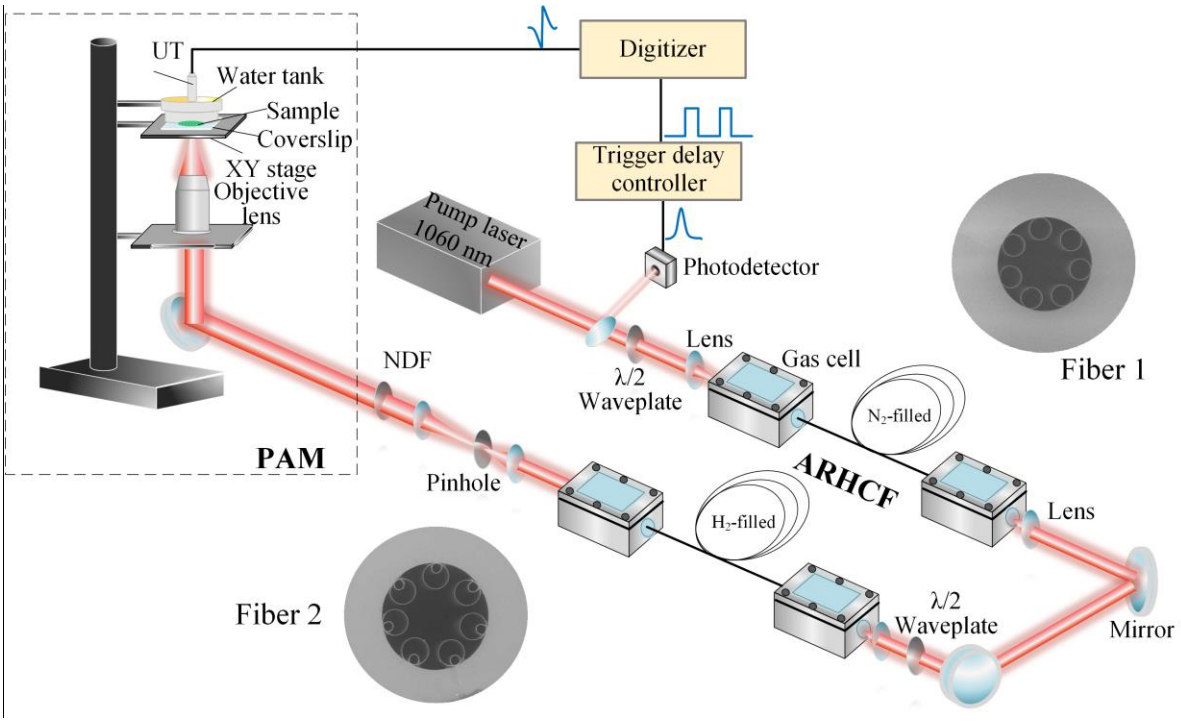


**Fig. 1 Overall MIR-PAM system.** The system consists of two-stage cascaded gas-filled ARHCF laser followed by a transmission mode PAM. Fiber 1 and Fiber 2: SEM images of the 1st and 2nd stage ARHCFs, respectively. ARHCF: anti-resonant hollow-core fiber. NDF: neutral density filter. UT: ultrasound transducer. PAM: photoacoustic microscopy.

forming a negative-curvature core shape with an inner jacket tube diameter of 32.8 μm. The simulated loss spectrum of the fiber is shown in Fig. S1 (a), with a loss value of ~0.02 dB/m at 1060 nm and ~0.05 dB/m at 1409 nm [35]. The 2$^{nd}$ stage ARHCF (Fiber 2 in Fig. 1) is 5 meters long with a nested cladding structure and a core diameter of 82 μm [36]. The diameter for external and internal capillaries are 40.3 μm and 13.6 μm, and the wall thickness are 987 nm and 1.37 μm, respectively. This ARHCF has a loss of only ~0.004 dB/m at 3409 nm (see Fig. S1 (b)), which is a critical condition for the efficient generation of the 3.4 μm Raman laser. In addition, the nested structure of the 2$^{nd}$ ARHCF significantly suppresses the bend loss and therefore allows a bending

bioRxiv preprint doi: https://doi.org/10.1101/2024.04.02.587715; this version posted April 2, 2024. The copyright holder for this preprint (which was not certified by peer review) is the author/funder. All rights reserved. No reuse allowed without permission.

diameter of ~40 cm facilitating the development of a compact PAM system. The 1st ARHCF can be also coiled with ~40 cm diameter without high bending loss due to the small core diameter [37].

### *2.2 Mid-infrared photoacoustic microscopy*

The generated 3.4 μm Raman laser beam is then expanded and coupled into the PAM. The output energy is properly attenuated by using a neutral density filter (NDF, Thorlabs, NDC-50C-2M) to avoid the sample damage. The beam is focused by a reflected IR objective lens (PIKE, 40x, 0.78 NA) which has a designed obscuration of 42.9%. The PAM is performed in a transmission mode, and the sample is placed above a transparent sapphire-based coverslip (#18-471, Edmund Optics). Then a water tank with a flat polymer bottom surface (μ-Dish, Ibidi) with 200 μm thickness is placed tightly above the sample to fix and flatten the sample surface and to couple the acoustic signal into the distilled water filled in the tank. The water tank and the sample are combined as an integrated part held by a high-resolution XY stage (8MTF-75LS05, Standa) driven by a stepper & DC motor controller (8SMC5-USB, Standa) to enable the sample scanning with a minimum step size < 10 nm, and a maximum speed of 35000 steps/s. A focused immersive ultrasound transducer (UT, Precision Acoustic) with a central frequency of 20 MHz is immersed within the distilled water in the tank. The UT has an acoustic focal length of 8 mm and a diameter of 10 mm and is coaxially aligned with the reflective IR objective lens. The detected PA signals are filtered by two analog filters (Mini-circuits, 1 MHz long pass filter and 27 MHz low pass filter), then amplified by a low-noise wideband amplifier (Spectrum Instrumentation) and finally received with a high-speed digitizer (M4i.4421-x8, Spectrum Instrumentation) for data processing. The digitizer, integrated in a computer, operates at 250 MS/second sampling rate with a voltage resolution of 16 bits.

bioRxiv preprint doi: https://doi.org/10.1101/2024.04.02.587715; this version posted April 2, 2024. The copyright holder for this preprint (which was not certified by peer review) is the author/funder. All rights reserved. No reuse allowed without permission.

An external trigger delay controller (AeroDiode) synchronizes the scanning and data acquisition. A small fraction of the pump pulse energy is extracted from the pump beam and is recorded by a NIR photodetector (DET08C/M, Thorlabs) as a trigger signal, as shown in Fig. 1. Then the output signal from the photodetector is connected to the input side of a trigger delay controller as the input trigger signal. Once the trigger delay controller detects the pump pulse signal, a square signal is generated and acts as the PA trigger for X-Y stage movement and signal synchronization. The PA signal is recorded ~5 μs after the laser pulse and ~0.2 μs after the square trigger signal at a repetition rate of 1.2 kHz. During the sample scanning, to minimize noises and enhance signal to noise ratio, 100 pulses (A-lines) are averaged corresponding to a ~83 ms dwell time.

### *2.3 Brain sample preparation*

In order to investigate the performance of our MIR-PAM in real brain tissue, wild-type adult mice were employed. The procedure to prepare the brain slices presented below is approved by the Animal Experiments Inspectorate under the Danish Ministry of Food, Agriculture, and Fisheries, and all procedures adhere to the European guidelines for the care and use of laboratory animals, EU directive 2010/63/EU. A Long-Evans wild-type adult rat was anesthetized by intraperitoneal injection of 200 mg/kg sodium pentobarbital. Hereafter, the level of anesthesia was assessed by pedal reflex pain response to firm toe pinch. Once a sufficient level of anesthesia was reached, the chest cavity was opened to expose the heart. A catheter, connected to a peristaltic pump (Gilsion, minipuls3), was inserted into the left ventricle of the heart, and a small incision was made into the vena cava inferior for perfusion. The perfusion of the rat was performed with 30 ml of 1X phosphate-buffered saline (PBS) followed by 30 ml of 4% paraformaldehyde (PFA) at the rate of 7.8 ml $min^{-1}$. The rat was subsequently decapitated using a guillotine. The brain was dissected out and directly put into ice-cold 4% PFA. After fixation for 4 h at 4 °C, the brain was transferred to

bioRxiv preprint doi: https://doi.org/10.1101/2024.04.02.587715; this version posted April 2, 2024. The copyright holder for this preprint (which was not certified by peer review) is the author/funder. All rights reserved. No reuse allowed without permission.

30% sucrose (w/v) for cryoprotection at 4 °C. A vibratome (LEICA, VT1200) was then used to section the brain into slices. To facilitate sectioning, the brain was embedded in 3% agarose gels prepared with a method similar to the one for preparing the 0.6% gels described above. The slicing was conducted in ice-cold 1X PBS. A similar process has been also followed in [38]. The brain slice has a thickness of 400 μm. During the PAM imaging, the slice is kept in 1X PBS at room temperature.

## 3 Results and discussion

### *3.1 Gas-filled hollow-core fiber laser source*

Figure 2 (a) presents the spectra of the pump laser as well as Raman Stokes lines, measured using an infrared spectrometer (Spectro320 Instrument Systems) with a resolution of 0.14 nm. The gaussian-like beam profile of the 1$^{st}$ Raman pulse, measured by a beam profiler (BP109-IR2, Thorlabs), indicates that the Raman laser operates at the fundamental mode. To maximize the output pulse energy, first, we measured the pulse energy of the 1409 nm Raman line output of the 1st stage ARHCF in terms of the $N_2$ pressure [35]. The Raman line appears at 9 bar pressure and the pulse energy reaches its maximum of up to ~26.5 μJ at ~15 bar pressure, corresponding to a quantum efficiency of 45%.

By pumping the 1409 nm Raman line into the 2$^{nd}$ stage ARHCF, a Raman line at 3.4 μm wavelength is observed when the pressure is > 5 bar, as seen in Fig. 2 (a), with a linewidth of ~1 nm. The average power of the 3.4 μm Raman laser was measured by extracting it from the residual 1.4 μm pump using a 2400 nm long-pass filter (FELH2400, Thorlabs, transmission 98% at 3.4 μm). Figure 2 (b) shows the pulse energy evolution of the 3.4 μm Raman laser, as well as the total energy including both the Raman laser and residual pump at 1409 nm without using a filter, as a

bioRxiv preprint doi: https://doi.org/10.1101/2024.04.02.587715; this version posted April 2, 2024. The copyright holder for this preprint (which was not certified by peer review) is the author/funder. All rights reserved. No reuse allowed without permission.

function of the $H_2$ pressure. The Raman pulse energy begins to rise at ~5 bar, with the highest value to be 2.75 μJ at ~20 bar. As the pressure further increases, the energy starts to decrease slightly, because the Raman laser reaches its maximal pulse energy at a shorter fiber length. The long-term stability and noise performance of the Raman laser source were also characterized, to provide a reference for implementing the subsequent PAM application. The noise performance of the MIR Raman pulses was measured in term of the relative intensity noise (RIN) of pulse peak intensity at 20 and 29 bar, using a photodetector (100 MHz bandwidth, PDAVJ8, Thorlabs) connected to an oscilloscope (6 GHz bandwidth, MSO64B, Tektronix). Figure 2 (c) shows the

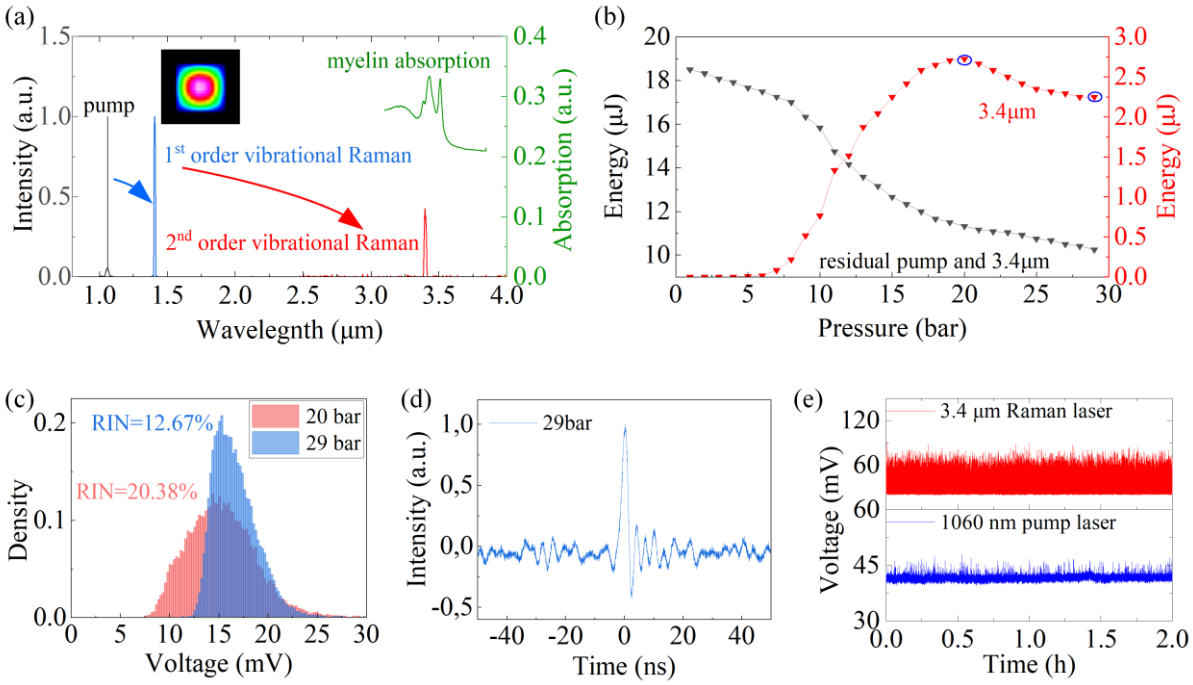


**Fig. 2. Characterization of the gas-filled ARHCF laser source. (a)** Measured spectra including the pump line and Raman lines generated from the cascaded ARHCFs. The right axis shows the absorption spectrum of myelin extracted from [10]. Inset: beam profile of 1st Raman pulse at 1409nm. **(b)** Pulse energy evolution of the 3.4 μm Raman pulse as a function of $H_2$ pressure. **(c)** Histograms of the pulse peak intensity of the 3.4 μm Raman pulse at 20 bar and 29 bar, respectively. **(d)** Pulse profile of the 3.4 μm Raman laser. **(e)** Pulse peak intensity monitoring of the 1060 nm pump and the 3.4 μm Raman lasers over 2 hours.

bioRxiv preprint doi: https://doi.org/10.1101/2024.04.02.587715; this version posted April 2, 2024. The copyright holder for this preprint (which was not certified by peer review) is the author/funder. All rights reserved. No reuse allowed without permission.

distribution of the measured histograms. At 20 bar pressure, the distribution has a gaussian-like profile with a RIN of 20.38%. Compared to 20 bar, at 29 bar pressure although the pulse energy slightly decreases to 2.25 μJ, a lower RIN of 12.67% is obtained. This is because, the SRS process becomes more efficient towards higher $H_2$ pressure due to the further suppression of transient SRS regime [39]. Given this property, here we set the pressure of $H_2$ to 29 bar, to better mitigate the acoustic signal fluctuation in the PAM application. Figure 2 (d) shows a typical pulse profile of the 3.4 μm Raman laser. The pulse width is ~2 ns but the precision of this measurement is compromised because of the limited bandwidth of the MIR photodetector. This Raman laser also shows a good long-term stability, as indicated by the 2 hours monitoring results of the laser peak intensities of both the 3.4 μm Raman laser and its pump at 1060 nm.

### *3.2 Characterization of the MIR-PAM*

The lateral resolution of the PAM was first evaluated by imaging a sharp knife edge with a thickness of 100 μm. Figure 3 (a) shows the optical image (top) and the corresponding PAM image (bottom). The pulse energy before and after the objective lens are ~1.9 μJ and ~1 μJ respectively due to the 42.9% obscuration. The PAM images are obtained with a step size of 1.25 μm after averaging 100 pulses. The edge spread function (ESF) is acquired from the averaged raw data of the intensity, and the line spread function (LSF) is then calculated and fitted from the differential of the ESF, as shown in Fig. 3 (b). From the full width at half maximum (FWHM) of LSF, the lateral resolution of our MIR-PAM is estimated to be ~12.36 μm.

The axial resolution $R_a$ is estimated experimentally by the pulse width of the impulse response of a single PA signal. Figure 3 (c) shows the PA signal and its envelope after Hilbert Transformation (HT). The axial resolution is extracted from the FWHM of the envelope, which is 62 ns, corresponding to 95.5 μm in distance, given the propagation velocity of sound in the sample

bioRxiv preprint doi: https://doi.org/10.1101/2024.04.02.587715; this version posted April 2, 2024. The copyright holder for this preprint (which was not certified by peer review) is the author/funder. All rights reserved. No reuse allowed without permission.

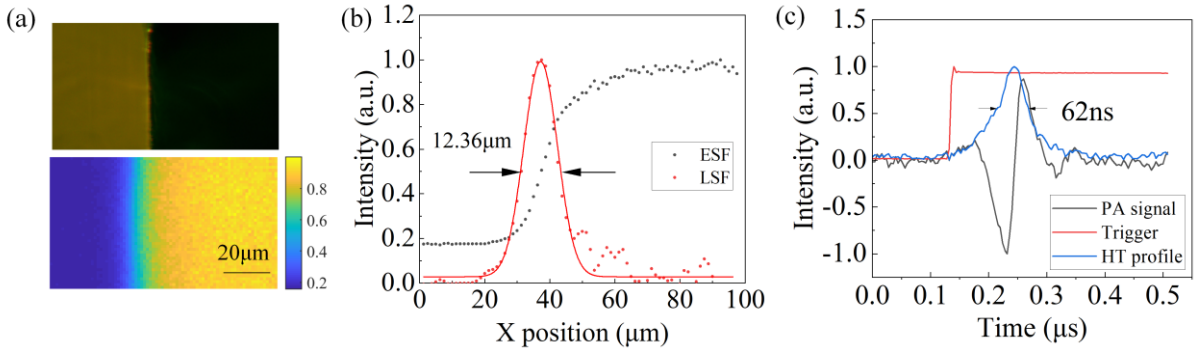


**Fig. 3 Resolution characterization of the MIR-PAM. (a)** Optical and photoacoustic images of a sharp blade edge. **(b)** Fitted ESF and LSF extracted from PA image in (a). **(c)** Single PA signal and its Hilbert transformation (HT) profile.

of $c$=1540 m/s [40]. The axial resolution can also be numerically calculated by the velocity of the acoustic signal and the central frequency of the ultrasound transducer as $R_a$=0.88$c$/$B$, where $B$ is the central frequency of the UT. In our case, the theoretical axial resolution is ~67.8 μm.

### *3.3 Ex-vivo PAM*

Figure 4 (a) shows the *ex-vivo* PAM image of the mouse brain slice with the thickness of 400 μm obtained through using the proposed 3.4 μm laser as light source. The scanning step size is 40 μm and the total scanning time is ~40 min. HT was used for extracting the absolute amplitude of the acoustic signal, and then the image is post-processed by Gamma transformation and a contrast enhancement of 0.5% saturation using ImageJ software. In comparison with the optical image in Fig. 4 (b), we can clearly see the outlines of the different brain regions. The myelin-rich regions, such as corpus callosum, are brighter than other regions. Small structures like mammillothalamic fasciculus (mtf) and fornix (fo) can also be distinguished, exhibiting as bright spots, since they consist of heavily myelinated fibers [10,41,42]. These characteristics are invisible in the optical image shown in Fig. 4 (b). The regions with less myelin, such as hippocampus, which mainly

bioRxiv preprint doi: https://doi.org/10.1101/2024.04.02.587715; this version posted April 2, 2024. The copyright holder for this preprint (which was not certified by peer review) is the author/funder. All rights reserved. No reuse allowed without permission.

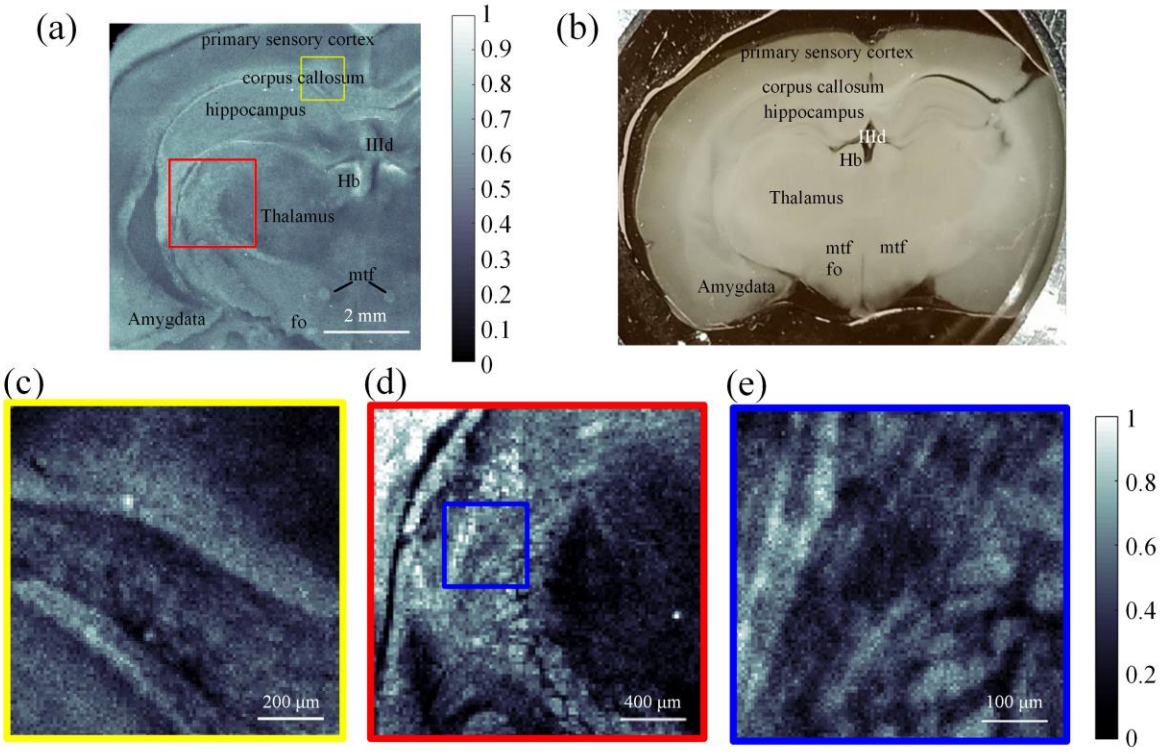


**Fig. 4 Image of the mouse brain. (a)** *Ex-vivo* PA image of the mouse brain slice. Hb: habenular nuclei. IIId: IIIrd ventricle. mtf: mammillothalamic fasciculus. fo: fornix. **(b)** Optical image of the mouse brain slice. **(c)** Enlarged view of the structure in the yellow box in (a) with a scanning step size of 10 μm. **(d)** Enlarged view of the structure in the red box in (a) with a scanning step size of 20 μm. **(e)** Enlarged view of the structure in the blue box in (d) with a scanning step size of 5 μm.

consists of gray matter, appear to be darker. Finally, due to the lack of myelin, the cavity structure (lateral ventricle IIId) looks like a void with clear boundaries.

Enlarged views of the corpus callosum and thalamus regions were scanned with a step size of 10 μm and 20 μm respectively, as shown in Fig. 4 (c) and (d). The border between corpus callosum and hippocampus is clearly visible in Fig. 4 (c). In Fig. 4 (d), patterns with a fish-scale-like appearance are observable, which agree with other brain images reported in the literature [10]. A further enlargement of the thalamus region, performed with a scanning step of 5 μm, is shown in Fig. 4 (e). Here, we can observe some thick nerve fiber bundles, which has been also verified and

bioRxiv preprint doi: https://doi.org/10.1101/2024.04.02.587715; this version posted April 2, 2024. The copyright holder for this preprint (which was not certified by peer review) is the author/funder. All rights reserved. No reuse allowed without permission.

observed by other MIR-PAMs [10,13], demonstrating the ability of our new MIR-PAM Raman fiber laser for lipid-rich myelin imaging. All enlarged images required a scanning time of about 20 min.

## 4 Conclusion

This work aims to create a new avenue of the emerging gas-filled Raman laser technology for MIR-PAM. As a proof-of-concept, a high-energy Raman laser at ~3.4 μm was developed and employed for brain imaging. This work can be further extended to multispectral PAM through operating the gas-filled fiber laser with the reconfigurable multiple spectral lines spanning from near- to mid-infrared region [36].

On the other hand, although this work still involves the free-spacing coupling to ARHCF, an all-fiber structure will be expected in our future work, given the recent progress on the low-loss splicing of ARHCFs [43-45].

### *Disclosures*

The authors declare that there are no conflicts of interest.

### *Code, Data, and Materials*

The data of this work is available from the corresponding author upon reasonable request.

### *Acknowledgments*

This work is supported by LUNDBECK FONDEN (Grant No. R346-2020-1924, No. R276-2018-869), VILLUM Fonden (Grant No. 36063, Grant No. 40964), and US ARO (Grant No. W911NF-19-1-0426).

bioRxiv preprint doi: https://doi.org/10.1101/2024.04.02.587715; this version posted April 2, 2024. The copyright holder for this preprint (which was not certified by peer review) is the author/funder. All rights reserved. No reuse allowed without permission.

## *References*


1. Dasa MK, et al., High-pulse energy supercontinuum laser for high-resolution spectroscopic photoacoustic imaging of lipids in the 1650-1850 nm region. Biomedical Optics Express 2018;9:1762–70.
2. Nteroli G, et al., Two octaves spanning photoacoustic microscopy. Scientific Reports 2022;12:10590.
3. Ntziachristos V, et al., Looking and listening to light: the evolution of whole-body photonic imaging. Nature Biotechnology 2005;23:313–20.
4. Wang LV. Multiscale photoacoustic microscopy and computed tomography. Nature Photonics 2009;3:503–9.
5. Cai D, et al., Dual-view photoacoustic microscopy for quantitative cell nuclear imaging. Optics Letters 2018;43:4875–8.
6. Gottschalk S, et al., Rapid volumetric optoacoustic imaging of neural dynamics across the mouse brain. Nature Biomedical Engineering 2019;3:392–401.
7. Nguyen VP, et al., Contrast agent enhanced multimodal photoacoustic microscopy and optical coherence tomography for imaging of rabbit choroidal and retinal vessels in vivo. Scientific Reports 2019;9:5945.
8. Liu C, et al., Five-wavelength optical-resolution photoacoustic microscopy of blood and lymphatic vessels. Advanced Photonics 2021;3:016002–016002.
9. Li C, et al., High-energy all-fiber gain-switched thulium-doped fiber laser for volumetric photoacoustic imaging of lipids. Photonics Research 2020;8:160–4.
10. He Y, et al., Label-free imaging of lipid-rich biological tissues by mid-infrared photoacoustic microscopy. Journal of Biomedical Optics 2020;25:106506–106506.
11. Pleitez MA, et al., Label-free metabolic imaging by mid-infrared optoacoustic microscopy in living cells. Nature Biotechnology 2020;38:293–6.

bioRxiv preprint doi: https://doi.org/10.1101/2024.04.02.587715; this version posted April 2, 2024. The copyright holder for this preprint (which was not certified by peer review) is the author/funder. All rights reserved. No reuse allowed without permission.

12. Ko V, et al., Fast histological assessment of adipose tissue inflammation by label-free mid-infrared optoacoustic microscopy. Npj Imaging 2023;1;3.
13. Shi J, et al., High-resolution, high-contrast mid-infrared imaging of fresh biological samples with ultraviolet-localized photoacoustic microscopy. Nature Photonics 2019;13:609–15.
14. Gasparin F, et al., Protein-structure-sensitive mid-infrared optoacoustic microscopy enables label-free assessment of drug therapy in myeloma cells. bioRxiv 2024;0221:581391.
15. Yuan T et al., Functional live-cell mid-infrared microscopy and spectroscopy by optoacoustic and optothermal detection. Proc. SPIE 12392, Advanced Chemical Microscopy for Life Science and Translational Medicine 2023; 1239202.
16. Visscher M, et al., Label-free analytic histology of carotid atherosclerosis by mid-infrared optoacoustic microscopy. Photoacoustics 2022;26:100354.
17. Buma T, et al., Near-infrared multispectral photoacoustic microscopy using a graded-index fiber amplifier. Photoacoustics 2016;4(3):83-90.
18. Lee H, et al., Nanosecond SRS fiber amplifier for label-free near-infrared photoacoustic microscopy of lipids. Photoacoustics 2022;25:100331.
19. Buma T, et al., Multispectral photoacoustic microscopy of lipids using a pulsed supercontinuum laser. Biomed Opt Express. 2017; 9(1):276-288.
20. Cho S, et al., Efficient label-free in vivo photoacoustic imaging of melanoma cells using a condensed NIR-I spectral window. Photoacoustics 2023;29:100456.
21. Wang Y, et al., Mid-infrared photoacoustic gas monitoring driven by a gas-filled hollow-core fiber laser. Scientific Reports 2021;11:3512.
22. Markos C, et al., Hybrid photonic-crystal fiber. Reviews of Modern Physics 2017;89:045003.
23. Bache M, et al., Poor-man's model of hollow-core anti-resonant fibers. Journal of the Optical Society of America B 2019;36:1;69-80.
24. Russell PSJ, et al., Hollow-core photonic crystal fibres for gas-based nonlinear optics. Nature Photonics 2014;8:278.

bioRxiv preprint doi: https://doi.org/10.1101/2024.04.02.587715; this version posted April 2, 2024. The copyright holder for this preprint (which was not certified by peer review) is the author/funder. All rights reserved. No reuse allowed without permission.

25. Couny F, et al., Generation and Photonic Guidance of Multi-Octave Optical-Frequency Combs. Science 2007;318:1118–21.
26. Krupa K, et al., Intense stimulated Raman scattering in $CO_2$-filled hollow-core fibers. Optics Letters 2019;44:5318–21.
27. Astapovich MS, et al., Efficient 4.42 μm Raman laser based on hollow-core silica fiber, Applied Photonics 2018.
28. Edelstein S, et al., High-efficiency Raman conversion in $SF_6$-and $CF_4$-filled hollow-core photonic bandgap fibers. Optics Letters 2019;44:5856–9.
29. Wang Y, et al., $CO_2$-based hollow-core fiber Raman laser with high-pulse energy at 1.95 μm. Optics Letters 2021;46:5133–6.
30. Adamu AI, et al., Multi-wavelength high-energy gas-filled fiber Raman laser spanning from 1.53 μm to 2.4 μm. Optics Letters 2021;46:452–5.
31. Adamu AI, et al., Deep-UV to Mid-IR Supercontinuum Generation driven by Mid-IR Ultrashort Pulses in a Gas-filled Hollow-core Fiber. Scientific Reports 2019;9:4446.
32. Cassataro M, et al., Generation of broadband mid-IR and UV light in gas-filled single-ring hollow-core PCF. Optics Express 2017;25:7637–44.
33. Adamu AI, et al., Noise and spectral stability of deep-UV gas-filled fiber-based supercontinuum sources driven by ultrafast mid-IR pulses. Scientific Reports 2020;10:4912.
34. William KB, et al., Wavelength dependence of the absolute Raman gain coefficient for the Q(1) transition in $H_2$, Journal of the Optical Society of America B 1986;3:677-682.
35. Hong L, et al., High energy and narrow linewidth $N_2$-filled hollow-core fiber laser at 1.4 μm, 2023, arXiv:2312.03581.
36. Wang Y, et al., Synthesizing gas-filled fiber Raman lines enables access to the molecular fingerprint region, 2023, arXiv:2311.15987.
37. Frosz MH, et al., Analytical formulation for the bend loss in single-ring hollow-core photonic crystal fibers, Photonics Research 2017;5:88-91.

bioRxiv preprint doi: https://doi.org/10.1101/2024.04.02.587715; this version posted April 2, 2024. The copyright holder for this preprint (which was not certified by peer review) is the author/funder. All rights reserved. No reuse allowed without permission.


38. Sui K, et al., Adaptive polymer fiber neural device for drug delivery and enlarged illumination angle for neuromodulation. Journal of Neural Engineering 2022;19:016035.
39. Wang Y, et al., Noise Performance and Long-Term Stability of Near- and Mid-IR Gas-Filled Fiber Raman Lasers, Journal of Lightwave Technology 2021;39:11.
40. Jeon S, et al., Review on practical photoacoustic microscopy. Photoacoustics 2019;15:100141.
41. Schröder H, et al., In: Schröder H, Moser N, Huggenberger S, editors. Neuroanatomy of the Mouse: An Introduction, Cham: Springer International Publishing; 2020;305–18.
42. Patestas MA, et al., A Textbook of Neuroanatomy (2nd ed.). Hoboken, New Jersey: Wiley-Blackwell 2016; 434.
43. Li Z, et al., Efficient mid-infrared cascade Raman source in methane-filled hollow-core fibers operating at 2.8 μm. Optics Letters 2018;43: 4671-4674.
44. Dadashzadeh N, et al., Near diffraction-limited performance of an OPA pumped acetylene-filled hollow-core fiber laser in the mid-IR. Optics Express 2017;25:13351.
45. Cao L, et al., High peak power 2.8 μm Raman laser in a methane-filled negative-curvature fiber. Optics Express 2018;26:5609.
46. Cui Y, et al., 4.3 μm fiber laser in $CO_2$-filled hollow-core silica fibers. Optica 2019;6:951.
47. Aghbolagh FBA, et al., Mid IR hollow core fiber gas laser emitting at 4.6 μm. Optics Letters 2019;44:383.
48. Xu M, et al., Mid-infrared 1 W hollow-core fiber gas laser source. Optics Letters 2017;42:4055.
49. Astapovich MS, et al., Efficient 4.42 μm Raman laser based on hollow-core silica fiber. arXiv:1801.01729 (2017).
50. Gladyshev AV, et al., 2.9, 3.3, and 3.5 μm Raman Lasers Based on Revolver Hollow-Core Silica Fiber Filled by $1H_2/D_2$ Gas Mixture. IEEE Journal of Selected Topics in Quantum Electronics 2018;24:0903008.
51. Gladyshev AV, et al., 4.4-μm Raman laser based on hollow-core silica fibre. Quantum Electronics 2017;47:491.

bioRxiv preprint doi: https://doi.org/10.1101/2024.04.02.587715; this version posted April 2, 2024. The copyright holder for this preprint (which was not certified by peer review) is the author/funder. All rights reserved. No reuse allowed without permission.

359 52. Wang Y, et al., High pulse energy and quantum efficiency mid-infrared gas Raman fiber laser
360 targeting $CO_2$ absorption at 4.2 μm. Optics Letters 2020;45:1938-1941.
361 53. Zhou Z, et al., 3.1 W mid-infrared fiber laser at 4.16 μm based on HBr-filled hollow-core silica
362 fibers. Optics Letters 2022;47:5785-5788.
363 54. Huang W, et al., 4.5 W mid-infrared light source based on acetylene-filled hollow-core fibers. Optics
364 & Laser Technology 2022;151:108090.

bioRxiv preprint doi: https://doi.org/10.1101/2024.04.02.587715; this version posted April 2, 2024. The copyright holder for this preprint (which was not certified by peer review) is the author/funder. All rights reserved. No reuse allowed without permission.

# Supplementary Material

# Mid-infrared photoacoustic brain imaging enabled by cascaded gas-filled hollow-core fiber lasers

Cuiling Zhang,[a] Kunyang Sui,[a,b] Marcello Meneghetti,[a,b] Jose Enrique Antonio-Lopez,[c] Manoj K. Dasa,[d] Rune W. Berg,[b] Rodrigo Amezcua-Correa,[c] Yazhou Wang,[a] and Christos Markos,[a,e]

[a]*DTU Electro, Technical University of Denmark, 2800 Kgs. Lyngby, Denmark*

[b]*Department of Neuroscience, University of Copenhagen, 2200 Copenhagen, Denmark*

[c]*CREOL, The College of Optics and Photonics, University of Central Florida, Orlando, Florida 32816, USA*

[d]*NKT Photonics A/S, Blokken 84, Birkerød DK-3460, Denmark*

[e]*NORBLIS ApS, Virumgade 35D, 2830 Virum, Denmark*

bioRxiv preprint doi: https://doi.org/10.1101/2024.04.02.587715; this version posted April 2, 2024. The copyright holder for this preprint (which was not certified by peer review) is the author/funder. All rights reserved. No reuse allowed without permission.

# SUPPLEMENTARY NOTE 1. State-of-the-art of MIR gas-filled anti-resonant hollow-core fiber (ARHCF) lasers

Table.1 State-of-the-art of MIR gas-filled ARHCF lasers

| Year | Author | Gas | Wavelength (μm) |
|---|---|---|---|
| 2018[43] | Z. Li, *et. al.* | $CH_4$ | 2.8 |
| 2017[44] | N. Dadashzadeh *et. al.* | $C_2H_2$ | 3.11, 3.17 |
| 2018[45] | L. Cao, *et. al.* | $CH_4$ | 2.8 |
| 2019[46] | Y. Cui, *et. al.* | $CO_2$ | 4.3 |
| 2019[47] | F. B. A. Aghbolagh, *et. al.* | $NO_2$ | 4.6 |
| 2017[48] | M. Xu, *et. al.* | $C_2H_2$ | 3.1 |
| 2017[49] | A. V. Gladyshev, *et. al.* | $H_2$ | 4.42 |
| 2018[50] | A. V. Gladyshev, *et. al.* | $H_2/D_2$ | 2.9, 3.3, 3.5 |
| 2019[51] | M. S. Astapovich, *et. al.* | $H_2$ | 4.4 |
| 2020[52] | Y. Wang, *et. al.* | $H_2$ | 4.2 |
| 2022[53] | Z. Zhou, *et.al.* | HBr | 4.16 |
| 2022[54] | W. Huang, *et.al.* | $C_2H_2$ | 3.1 |
| This work | C. Zhang, *et al.* | $N_2(1^{st})/H_2(2^{nd})$ | 3.4 |

bioRxiv preprint doi: https://doi.org/10.1101/2024.04.02.587715; this version posted April 2, 2024. The copyright holder for this preprint (which was not certified by peer review) is the author/funder. All rights reserved. No reuse allowed without permission.

# SUPPLEMENTARY NOTE 2. Loss spectrum of ARHCFs

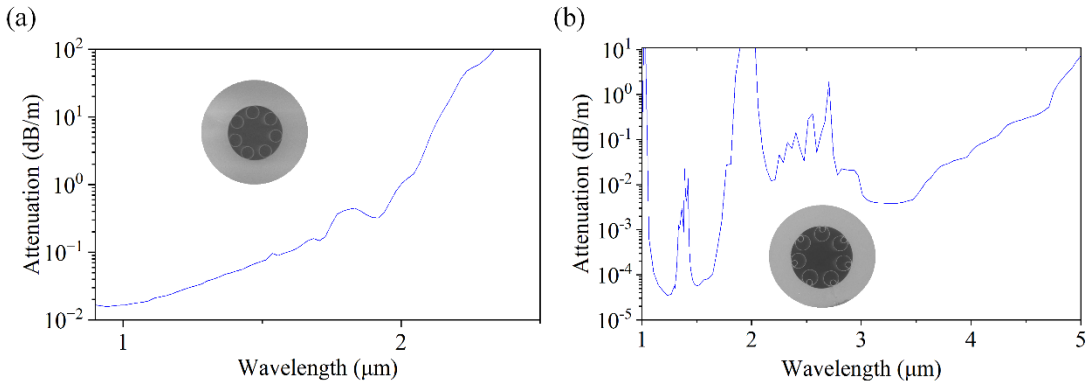


Fig. S1. Simulated attenuation spectra of **(a)** the first stage ARHCF and **(b)** the second stage ARHCF.

For the first stage ARHCF, the simulated attenuation coefficient is ~0.02 dB/m at 1060 nm and ~0.05 dB/m at 1409 nm, respectively. For the second stage ARHCF, the attenuation coefficient is ~0.005 dB/m at 1409 nm and ~0.004 dB/m at 3.4 μm, respectively.